Development of Ti-V-Nb-Cr-Mn High Entropy Alloys for Hydrogen Storage

Leandro Bernardes Serrano, Maria Moussa, Jie-Yi Yao, Gilbert Silva, Jean-Louis Bobet, Sydney Santos Ferreira, Regina Kátia

Development of Ti-V-Nb-Cr-Mn High Entropy Alloys for Hydrogen Storage

Leandro Bernardes Serrano[1], Maria Moussa[2], Jie-Yi Yao[3], Gilbert Silva[1], Jean-Louis Bobet[2], Sydney Santos Ferreira[4], Kátia Regina Cardoso[3]

[1]Universidade Federal de Itajubá - UNIFEI, Av. BPS, Itajubá – MG
[2]University of Bordeaux, CNRS, Bordeaux INP, ICMCB, UMR 5026, F-33600, Pessac France.
[3]Universidade Federal de São Paulo – UNIFESP, São José dos Campos - SP.
[4]Universidade Federal do ABC – UFABC - Santo André – SP.

Abstract

The development of novel high entropy alloys (HEA) of the TiVNbCrMn system for hydrogen storage is reported. The CALPHAD method was used to design alloys with a body centered cubic structures. Three alloy compositions, $Ti_{35}V_{35}Nb_{20}Cr_5Mn_5$; $Ti_{32}V_{32}Nb_{18}Cr_9Mn_9$; $Ti_{27.5}V_{27.5}Nb_{20}Cr_{12.5}Mn_{12.5}$, were fabricated by the arc melting process and characterized by X-ray diffraction (XRD) and SEM techniques. The activation behavior during the 1st hydrogen absorption of these alloys was investigated at room temperature and 2 MPa of H_2 pressure. These alloys absorb hydrogen forming FCC hydrides with high capacities of 2.52, 2.12 and 3.45 wt.%, respectively. Activation kinetics and incubation times were distinct for each alloy's composition. Hydrogen absorption/desorption cycles were performed for two alloys showing promising results since the maximum capacity of the alloys has been maintained despite a reduction in absorption kinetics.

KEYWORDS: High Entropy alloys; Metal hydrides; Hydrogen Storage; CALPHAD simulations.

1. Introduction

Hydrogen has long been considered a clean fuel with no CO_2 emissions; however, the great challenge involved in the employment of hydrogen as a zero emission fuel is the safety and the compactness of the storage. The most compact and safest technique that

has been studied is the solid-state storage in the form of metal hydride, which works by chemisorption. Recently, high entropy alloys (HEA), containing hydride-forming elements, have been considered as hydrogen storage materials [1,2].

High entropy alloys (HEA) have been developed as multicomponent alloys in which the control of the mixture's configurational entropy and other parameters such as atomic size incompatibility, mixture enthalpy, valence electron concentration and electronegativity [3-6] have allowed the prediction and control of phases formed in different alloy compositions and systems [3,6-7]. The maximum mixing entropy is obtained when several elements are mixed in an equimolar fraction, which tends to stabilize a random solid solution [3,4]. Therefore, these alloys are generally based on multicomponent systems with equiatomic or quasi-equiatomic compositions but many reports have considered addition of low fraction of extra elements to optimize other properties of interest. [8,9].

The crystal structures, microstructural characteristics, and properties of HEA depend on their composition and the type and amount of alloying elements [12,13]. Addition of elements with large atomic radii such as V, Ti or Nb results in increase of both lattice parameters and lattice distortion, promoting the formation of less compact structures (body centered cubic structures (BCC) instead of face centered cubic structures (FCC)) or ordered compounds (such as the Laves phase in alloys with increasing Nb content) [12-14].

Interesting hydrogen storage properties have recently been reported for different multicomponent alloys containing titanium. One of the best results reported so far was that of Sahlberg *et al.* [15] who investigated the equimolar TiVZrNbHf alloy that is known to crystallize into a BCC structure. This alloy is composed by elements that are strong hydride-formers and have a large difference in atomic radio ($\delta = 6.82\%$). The alloy absorbed 2.7 wt.% H_2 at 300 °C, achieving an H/M ratio = 2.5, which is considerably higher when compared to conventional hydrides which typically have H/M = 2. The significant amount of hydrogen that can be absorbed by the TiVZrNbHf alloy was attributed to the transition from the BCC to a body centered tetragonal (BCT) phase during hydrogenation. This is the typical behavior of BCC alloys during hydrogenation, as in the case of alloys in the TiCrV system. In these alloys, hydrogenation begins with hydrogen entering solid solution at the octahedral sites of the BCC lattice. At some point, a metal hydride with a FCC structure with the hydrogen atoms occupying the tetrahedral

sites (in a CaF_2 structure type) is formed [21]. It has been suggested [15] that this unprecedented hydrogen storage capacity is an effect of the deformation of the HEA crystal lattice, which favors the occupation of both tetrahedral and octahedral sites by hydrogen. The increase in lattice deformation in a HEA may be the driving force to open new interstitial sites for hydrogen.

Recently, it was suggested by Nygard *et al.* [29] that hydrogen sorption properties in BCC multicomponent alloys might be related to the valence electron concentration (VEC). It was observed that the highest capacity (2 H/M) was reached with VEC < 4.75, whereas alloys with VEC > 5 presented reduced maximum capacity (H/M < 2.0). The equimolar TiVNbCr alloy with VEC = 5 showed a reversible hydrogen storage capacity of 1.96 wt. % at room temperature and moderate pressures without any activation procedure. The effect of VEC was more recently studied by Silva *et al.* [24] in three multicomponent alloys with BCC structure and with the same VEC. These alloys formed FCC hydrides at room temperature, showing rapid absorption kinetics and similar maximum hydrogen capacities of 2 H/M, despite the different chemical composition.

Other works have shown good results in alloys containing Laves phases [16,18,23]. Alloys in the CoFeMnTixVyZrz system with C14 Laves phase showed a hydrogen absorption capacity of 1.6 wt. % at room temperature [23], while the ZrTiVCrFeNi alloy produced by selective laser melting, in which the C14 Laves is the predominant phase, presented a maximum hydrogen capacity of 1.81 wt.% at 100 bar and 50 °C, after activation at 500 °C [18]. Edalati *et al*. [25] designed and produced by arc melting, the high-entropy alloy TiZrCrMnFeNi that presented 95 wt. % of C14 Laves phase. The alloy absorbed and desorbed 1.7 wt. % of hydrogen, reversibly at room temperature, with a fast kinetics and without any activation process, which is a characteristic of the C14 Laves phase.

These results show that multicomponent HEA with body-centered cubic phase (BCC) structures and/or Laves phases present numerous opportunities for the discovery of new materials with superior hydrogen storage properties related to practical applications. In this work, three alloy compositions of the TiVNbCrMn system were designed with the support of CALPHAD method to obtain solid solutions with a BCC structure, and possible control of the amount of Laves phase through heat treatment. The hydrogen storage properties in terms of hydrogen capacity, absorption and desorption kinetics and

cycling reversibility were evaluated and correlated with the microstructure and composition of the alloys.

2. Materials and Methods

2.1. Alloy designing and synthesis

The design of the alloy compositions was carried out by the CALPHAD method using the Thermo-Calc® software and the TCHEA4 database aiming to obtain solid solutions with BCC structure and different Laves phase fractions. The main objective of choosing the alloy components is to obtain the BCC phase using Nb, Ti and V in large quantity, which are stabilizers of this phase and hydride formers, combining with an increase of the transition elements Cr and Mn, for the formation of the secondary phase of the AB_2 type (Laves) and also help in the destabilization of hydrides in cycling. The chosen compositions that satisfied the criteria adopted for the alloy design were $Ti_{35}V_{35}Nb_{20}Cr_5Mn_5$; $Ti_{32}V_{32}Nb_{18}Cr_9Mn_9$ and $Ti_{27.5}V_{27.5}Nb_{20}Cr_{12.5}Mn_{12.5}$.

The three alloy compositions were fabricated by arc melting furnace, using bulk pieces of high purity elements as raw materials (at least 99.9% of purity). The alloys were melted under an argon atmosphere purified by the melting of a Ti getter to minimize oxygen content in the samples. To ensure the chemical homogenization the ingots, they were flipped over and remelted five times.

2.2. Structural Characterization

Samples in the as-cast condition were submitted to metallographic preparation for subsequent microstructural and phase characterizations. The samples were transversally cut from the ingots, embedded in a phenolic resin, and submitted to grinding with SiC abrasive papers (from 320 to 1200 grit) and polishing with alumina suspensions (1 µm and 0.3 µm) and colloidal silica suspension (OP-S). Samples were submitted to chemical attack with Keller reagent for 50s.

The structural characterization of alloy samples was performed by X-ray diffraction (XRD) using Rigaku diffractometer model Ultima IV with a Cu-Kα radiation. The XRD analyses were also performed on the hydrogenated samples. The XRD profiles were analyzed by the Rietveld method using the software General Structure Analysis System II (GSAS-II) to determine the lattice parameters and the fraction of phases [26].

The microstructural characterization of the as-cast alloys was performed by scanning electron microscopy (SEM) using a FEI microscope, model INSPECT S50, equipped with energy dispersive X-ray spectroscopy system (EDS) for the qualitative and quantitative chemical composition analysis.

2.3. Hydrogen sorption measurements

The evaluation of hydrogen storage properties was performed by volumetric method using an automated Sievert's type apparatus. Alloys samples were crushed using a mortar and pestle prior to testing. Samples of the three compositions were activated at room temperature and hydrogen pressure of 2 MPa. The desorption were done at 300°C under dynamic vacuum for 3 h. After activation (1st cycle of absorption/ desorption), the $Ti_{32}V_{32}Nb_{18}Cr_9Mn_9$ and the $Ti_{27.5}V_{27.5}Nb_{20}Cr_{12.5}Mn_{12.5}$ alloys were subjected to three more cycles of hydrogen absorption and release. These cycles were performed with the same parameters of the activation.

3. Results and discussion

3.1. CALPHAD – assisted alloy design

Design of alloys of interest was performed with the assistance of CALPHAD calculations via Thermo-Calc software. The calculated amount of equilibrium phases as function of temperature in the alloys of interest are shown in Figure 1. The simulations predicted a BCC solid solution as the predominant phase for all the investigated alloys. For the $Ti_{35}V_{35}Nb_{20}Cr_5Mn_5$ alloy (Figure 1a), a second BCC phase, with B2 structure, is predicted to form at low temperatures (below 450°C).

The thermodynamic calculations for the other two compositions predict the formation of a C14_ Laves phase with a hexagonal structure (space group $P6_3mmc$) in addition to the second BCC_B2 phase (which is an ordered phase structure of the CsCl type with space group Pm-3m), as indicated in their respective phase diagrams (Figures 1b and 1c). Although the BCC_A2 phase remains the main phase, in the $Ti_{32}V_{32}Nb_{18}Cr_9Mn_9$ and $Ti_{27.5}V_{27.5}Nb_{20}Cr_{12.5}Mn_{12.5}$ alloys, the increase in the Cr and Mn content results in an increase of the amount of BCC_B2 and Laves phases at low temperatures. The temperature of the beginning of formation of BCC_B2 and Laves phase also increases in the alloys with higher Cr and Mn content.

The BCC_A2 phase has the same calculated chemical composition at 800 °C in the $Ti_{35}V_{35}Nb_{20}Cr_5Mn_5$ and $Ti_{32}V_{32}Nb_{18}Cr_9Mn_9$ alloys. The calculated composition of the BCC_A2 and C14_Laves phase for the $Ti_{27.5}V_{27.5}Nb_{20}Cr_{12.5}Mn_{12.5}$ alloy at 800°C is shown in Table 1. These results indicate a BCC_A2 structure with the composition close to the nominal of the alloy and the C14_Laves with most of the Cr and Mn element, showing that the increase of Mn and Cr content favored the formation of this phase with multi-element composition of type (Nb, Ti)$(Mn,Cr)_2$.

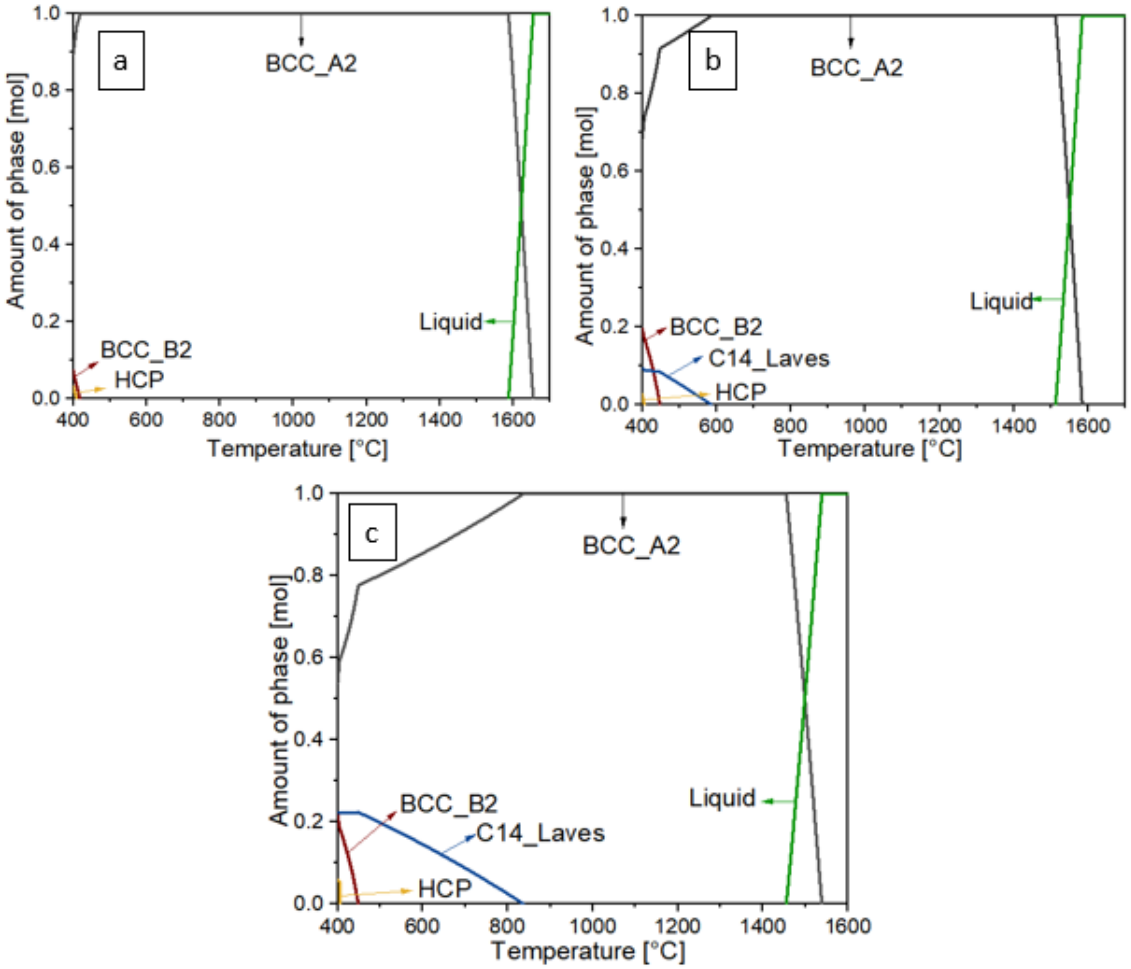

Figure 1- Phase diagram of (a) $Ti_{35}V_{35}Nb_{20}Cr_5Mn_5$, (b) $Ti_{32}V_{32}Nb_{18}Cr_9Mn_9$ and (c) $Ti_{27.5}V_{27.5}Nb_{20}Cr_{12.5}Mn_{12.5}$ calculated by CALPHAD method using Thermo-Calc software (TCHE4A database).

Table 1 - Chemical composition of BCC_A2 and C14_Laves phase at 800 ºC in the $Ti_{27.5}V_{27.5}Nb_{20}Cr_{12.5}Mn_{12.5}$ alloy calculated by Thermo-Calc software.

Phase	Ti (at.%)	V (at.%)	Nb (at.%)	Cr (at.%)	Mn (at.%)
BCC_A2	27.9	28.2	27.3	12.1	11.9
C14_Laves	10.9	0	24.4	28.3	36.3

3.2. Structural Characterization

The Figure 2 shows the X-ray diffractograms of the as-cast $Ti_{35}V_{35}Nb_{20}Cr_5Mn_5$ (a), $Ti_{32}V_{32}Nb_{18}Cr_9Mn_9$ (b) and $Ti_{27.5}V_{27.5}Nb_{20}Cr_{12.5}Mn_{12.5}$ (c) alloys. The XRD patterns present mainly peaks related to the BCC phase for the three alloys. In the alloy with the highest levels of Cr and Mn, $Ti_{27.5}V_{27.5}Nb_{20}Cr_{12.5}Mn_{12.5}$, low intensity peaks for 2θ = 36.6°, 38.3°, 91.5° and 95.5° also can be observed. These peaks are associated with the C14_ Laves phase, that has around 6 wt.% abundance based on the Rietveld refinement. Table 2 summarizes the crystal lattice parameters obtained from Rietveld refinement for the investigated alloys. The reduction of the lattice parameter of the BCC phase with the increase of the Cr and Mn contents in the alloys, can be directly observed in the X-ray diffractograms, by the shift of this phase's peaks to larger angles. Considering the smaller atomic radius of the Cr (24Å) and Mn (25Å), an increasing amount of them in composition, causes this difference in the lattice parameters and consequently in the cell volume values, from de 32.08 to 30.21 $Å^3$.

Table 2 - Lattices parameters and cell volume calculated by Rietveld refinement for the three alloys.

Composition	Structure	Lattices parameters (Å) a	c	cell volume $Å^3$	cell volume/Z
$Ti_{35}V_{35}Nb_{20}Cr_5Mn_5$	BCC	3.177	-	32.08	16.03
$Ti_{32}V_{32}Nb_{18}Cr_9Mn_9$	BCC	3.130	-	30.68	15.34
$Ti_{27.5}V_{27.5}Nb_{20}Cr_{12.5}Mn_{12.7}$	BCC Laves	3.135 5.001	- 8.226	30.81 178.19	15.40 29.70

. The $Ti_{27.5}V_{27.5}Nb_{20}Cr_{12.5}Mn_{12.5}$alloy presents peaks of the Laves phase in the X-ray diffractogram, this phase contains higher content of Cr and Mn, which could explain the

stability or even a small increase in the lattice parameter compared to $Ti_{32}V_{32}Nb_{18}Cr_9Mn_9$ alloy, since the added amount of Cr and Mn in the composition is no longer in the solid solution, but in the formation of the intermetallic.

The XRD results seem to indicate that alloys in the as cast condition are constituted by phases in equilibrium at high temperatures, at least above 800°C, i.e., the main BCC phase and a small quantity of Laves phase for the alloy with higher Cr and Mn contents. In agreement with the previous calculations, this behavior results from the high cooling rate in the arc melting process and probably also due to the low diffusivity of the constituent elements in high entropy alloys [27].

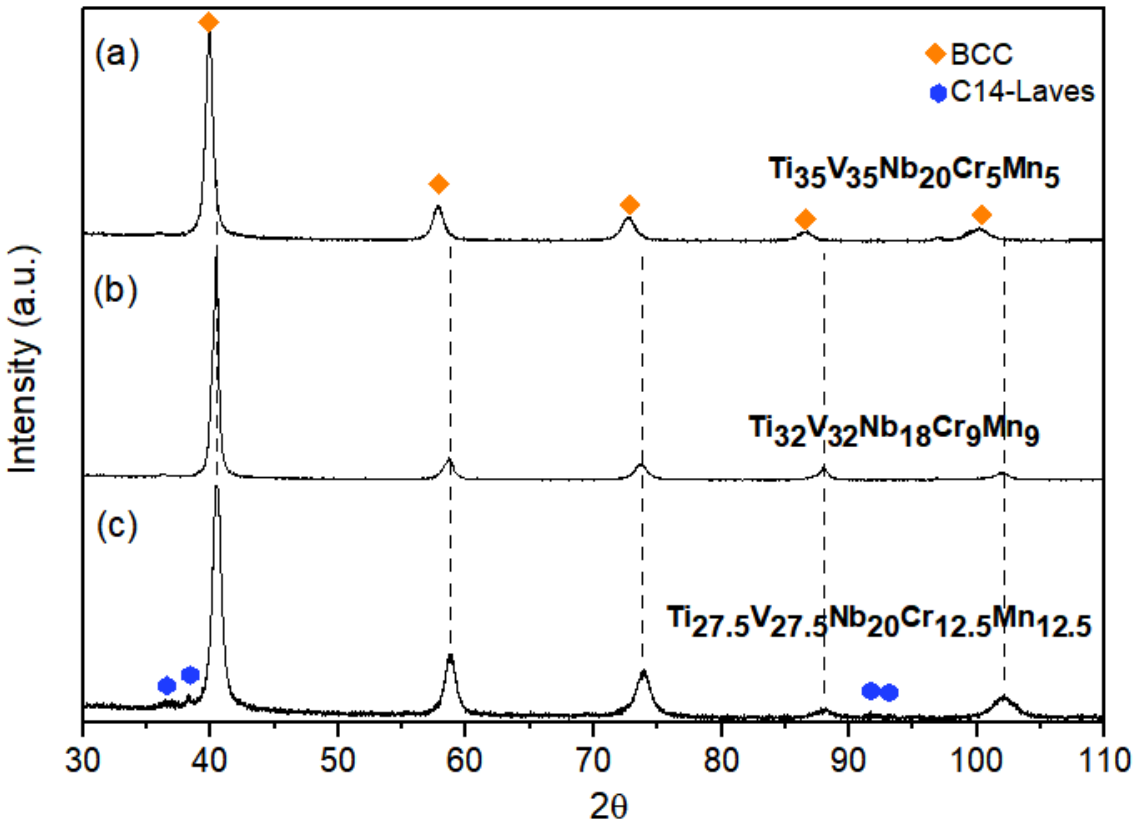

Figure 2 - X-ray diffraction patterns of the as-cast alloys, (a) $Ti_{35}V_{35}Nb_{20}Cr_5Mn_5$ (b) $Ti_{32}V_{32}Nb_{18}Cr_9Mn_9$ and (c) $Ti_{27.5}V_{27.5}Nb_{20}Cr_{12.5}Mn_{12.5}$.

Figure 3 shows SEM-BSE micrographs of the as-cast alloys. The three alloys, $Ti_{35}V_{35}Nb_{20}Cr_5Mn_5$, $Ti_{32}V_{32}Nb_{18}Cr_9Mn_9$ and $Ti_{27.5}V_{27.5}Nb_{20}Cr_{12.5}Mn_{12.5}$, present a dendritic microstructure with a clear contrast difference between the dendritic and interdendritic regions indicating a variation in the chemical composition.

The average chemical composition of the samples was determined by EDS analysis in large area (low magnification) while the chemical homogeneity of the samples was assessed by EDS measurements into the dendrite cores and into the interdendritic regions. The EDS results are summarized in Table 3. The interdendritic regions of the $Ti_{32}V_{32}Nb_{18}Cr_9Mn_9$ and $Ti_{27.5}V_{27.5}Nb_{20}Cr_{12.5}Mn_{12.5}$ alloys are enriched in Cr and Mn, but mainly in Ti. For the alloys with higher contents of Cr and Mn, the differences on the amount of these elements between the average composition and interdendritic regions becomes more evident. The $Ti_{35}V_{35}Nb_{20}Cr_5Mn_5$ alloy is the most homogeneous among the investigated ones. The average composition of the experimental alloys is close to its respective nominal composition, but with slightly lower Mn content (probably due to some evaporation during the arc melting process). The EDS analyses also indicate a lower Nb content than the nominal composition for the $Ti_{32}V_{32}Nb_{18}Cr_9Mn_9$ alloy. The inserts of the micrographs presented in Figure 3, shows small precipitates inside the interdentric region for all three alloys, acicular morphology for the $Ti_{35}V_{35}Nb_{20}Cr_5Mn_5$ and $Ti_{32}V_{32}Nb_{18}Cr_9Mn_9$ alloy, Figure 3a and 3b, globular precipitates for the $Ti_{27.5}V_{27.5}Nb_{20}Cr_{12.5}Mn_{12.5}$ alloy, Figure 3c, which must be related with the beginning of formation of a second phase, probably the Laves phase with Ti, because this element tend to leave the BCC solid solution first. The table in Figure 3c shows the composition of the two points indicated in the image (interdendritic precipitates) of the $Ti_{27.5}V_{27.5}Nb_{20}Cr_{12.5}Mn_{12.5}$ alloy. The highest levels of Ti, Cr and Mn, elements that form Laves phases, suggest the nucleation of this phase in these regions. These results indicate that the increase of Cr and Mn concomitant with the decrease of Ti in the alloys here studied, causes segregation of these elements to the interdendritic regions with a tendency to form the Laves phase in these regions.

Similar microstructures were found by Nygard *et al.* [29] in alloys with compositions, TiVNb, TiVCrNb and TiVCrMo. Nygard *et al.* also showed some mapping EDS, pointing out the segregation of Ti and Cr to the interdendritic region. In another work, Silva et al. [24] reported a similar behavior for the $(TiVNb)_{85}Cr_{15}$ alloy, which showed greater solubility for V and Nb in a BCC phase, as observed in the dendrite regions of the three alloys studied in this work (Table 3). Another work presented by Sleiman *et al.* [38] studied alloys with Ti, V and Nb. This paper, by evaluating the effect of Nb replacement by V in TiHfZrNbV alloys on the compositions of dendrites, interdendrites regions and

precipitates, it was shown that vanadium has a tendency to stabilize the BCC phase (dendrite) and in a greater amount tend to form the second phase in interdendritic regions.

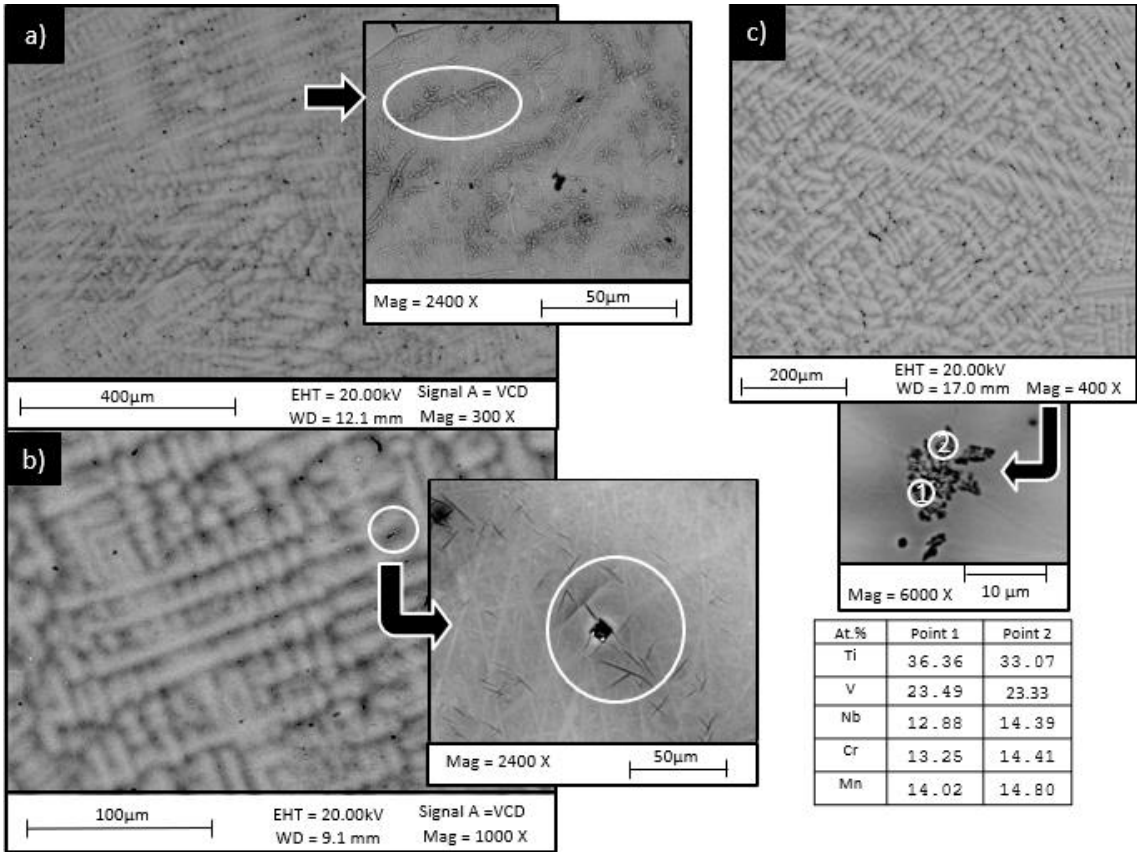

Figure 3 - SEM micrographs of (a) $Ti_{35}V_{35}Nb_{20}Cr_5Mn_5$, (b) $Ti_{32}V_{32}Nb_{18}Cr_9Mn_9$ and (c) $Ti_{27.5}V_{27.5}Nb_{20}Cr_{12.5}Mn_{12.5}$ with the composition of points 1 and 2 indicated in the insert assessed by EDS analyses. Micrographs show the dendritic microstructure, with precipitates in the interdendritic region in detail.

Table 3 - The chemical compositions of $Ti_{35}V_{35}Nb_{20}Cr_5Mn_5$, $Ti_{32}V_{32}Nb_{18}Cr_9Mn_9$ and $Ti_{27.5}V_{27.5}Nb_{20}Cr_{12.5}Mn_{12.5}$ measured by EDS.

System	**Composition**				
	Ti (%at.)	**V (%at.)**	**Nb (%at.)**	**Cr (%at.)**	**Mn (%at.)**
$Ti_{35}V_{35}Nb_{20}Cr_5Mn_5$ (general)	35.83	34.97	19.79	4.55	4.66
$Ti_{35}V_{35}Nb_{20}Cr_5Mn_5$ (dendrite)	35.91	34.95	19.72	4.76	4.68
$Ti_{35}V_{35}Nb_{20}Cr_5Mn_5$ (interdendrite)	35.86	34.40	19.94	5.05	4.76
$Ti_{32}V_{32}Nb_{18}Cr_9Mn_9$ (general)	33.79	33.00	15.86	9.24	8.11
$Ti_{32}V_{32}Nb_{18}Cr_9Mn_9$ (dendrite)	31.36	32.91	16.02	9.05	8.04
$Ti_{32}V_{32}Nb_{18}Cr_9Mn_9$ (interdendrite)	37.57	30.24	12.74	9.73	9.73
$Ti_{27.5}V_{27.5}Nb_{20}Cr_{12.5}Mn_{12.5}$ (general)	28.51	26.31	21.12	12.32	11.72
$Ti_{27.5}V_{27.5}Nb_{20}Cr_{12.5}Mn_{12.5}$ (dendrite)	28.60	26.18	21.05	12.36	11.81
$Ti_{27.5}V_{27.5}Nb_{20}Cr_{12.5}Mn_{12.5}$ (interdendrite)	33.07	23.33	14.39	14.41	14.80

The relative amount of the dendrites and the interdendrites areas was calculated by ImageJ software for the $Ti_{35}V_{35}Nb_{20}Cr_5Mn_5$ alloy and $Ti_{27.5}V_{27.5}Nb_{20}Cr_{12.5}Mn_{12.5.}$ An increase from 36,0% to 43,5% of the interdendritic areas was observed with the increase of Cr and Mn in the alloys. These elements may be segregated starting the formation of the C14 Laves with Nb and/or Ti, as suggested in Rietveld refinements for the $Ti_{27.5}V_{27.5}Nb_{20}Cr_{12.5}Mn_{12.5}$.

3.3. Hydrogen storage properties

Figure 4 presents the activation of the as-cat alloys under 2 MPa of H_2 at room temperature. Short incubations times were observed for $Ti_{35}V_{35}Nb_{20}Cr_5Mn_5$ and $Ti_{32}V_{32}Nb_{18}Cr_9Mn_9$ alloys that absorb hydrogen with low kinetics until reaching the saturation at 2.52 and 2.12 wt.% of hydrogen, respectively. Otherwise, the $Ti_{27.5}V_{27.5}Nb_{20}Cr_{12.5}Mn_{12.5}$ alloy presented a longer incubation time (450 min). After that, the hydrogenation of the alloy take place with faster kinetics until the saturation at 3.45 wt.%. This is the largest hydrogen storage capacity observed among the investigated alloys. Some works that have been published show that the formation of Laves_C14 phase can make the absorption kinetics faster and increase the number of absorption/desorption cycles. Edelati *et al.* [25] reported a high-entropy alloy TiZrCrMnFeNi containing 95 wt% of C14- Laves phase, which showed very fast kinetics at room temperature without any activation process. On the other hand, in a recent study, Liu *et al.* [9] compared two alloys containing low amounts of C14_Laves phase and showed that a limited amount of this phase can facilitate absorption kinetics by providing tunnels for diffusion, but when it is present in greater amounts it decreases the kinetics.

Therefore, the small content of Laves C14 phase formed in the $Ti_{27.5}V_{27.5}Nb_{20}Cr_{12.5}Mn_{12.5}$ alloy should be responsible for the sudden absorption after the incubation time.

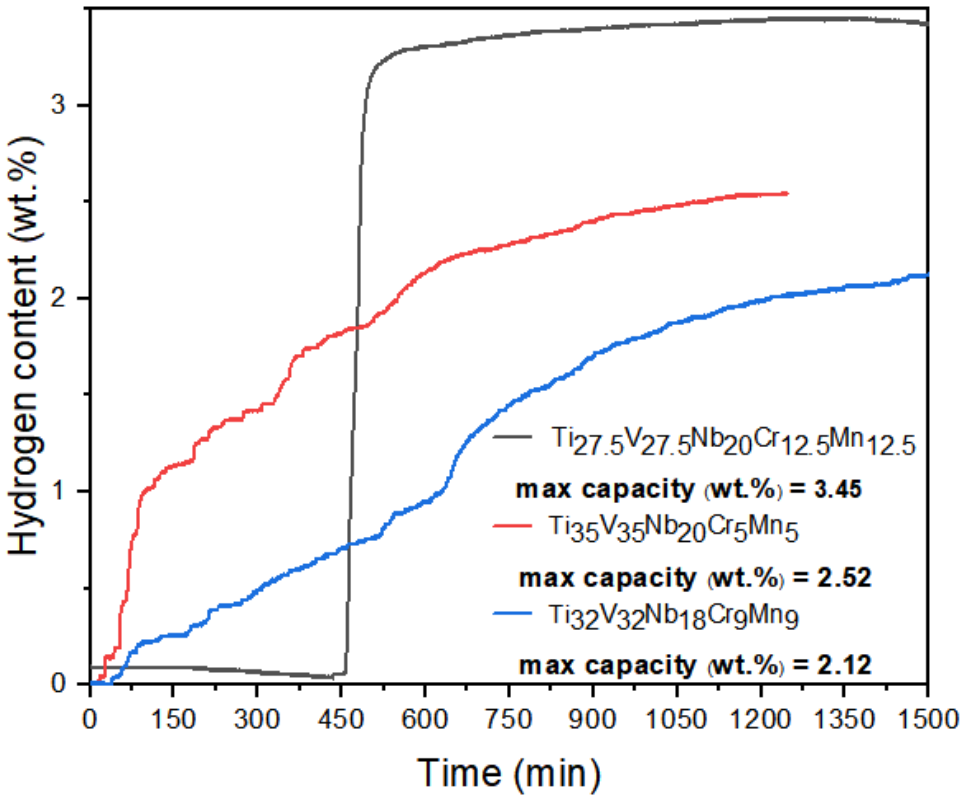

Figure 4. Activation curves and the maximum hydrogen absorption capacities of the as-cast alloys. Measurements under 2 MPa of H_2 at 25°C.

The XRD patterns of the activated $Ti_{35}V_{35}Nb_{20}Cr_5Mn_5$, $Ti_{32}V_{32}Nb_{18}Cr_9Mn_9$ and $Ti_{27.5}V_{27.5}Nb_{20}Cr_{12.5}Mn_{12.5}$ alloy are compared with as cast alloys in Figure 5. The hydrogenation of these alloys leads to the formation of FCC-hydrides whose lattice parameters are reported in Table 4. The lattice parameter of FCC hydride decreases from the $Ti_{35}V_{35}Nb_{20}Cr_5Mn_5$ to $Ti_{27.5}V_{27.5}Nb_{20}Cr_{12.5}Mn_{12.5}$ alloy, while for the original BCC phase it decreases from $Ti_{35}V_{35}Nb_{20}Cr_5Mn_5$ to $Ti_{32}V_{32}Nb_{18}Cr_9Mn_9$ and increases again for the $Ti_{27.5}V_{27.5}Nb_{20}Cr_{12.5}Mn_{12.5}$. The higher value of cell volume obtained by $Ti_{35}V_{35}Nb_{20}Cr_5Mn_5$ alloy confirms the higher hydrogen capacity of this alloy than $Ti_{32}V_{32}Nb_{18}Cr_9Mn_9$ in the 1st activation. The unit cell volume by Z expansion from the BCC structure to FCC phase was about 34%, 38,2% and 26,8% for the $Ti_{35}V_{35}Nb_{20}Cr_5Mn_5$, $Ti_{32}V_{32}Nb_{18}Cr_9Mn_9$ and the $Ti_{27.5}V_{27.5}Nb_{20}Cr_{12.5}Mn_{12.5}$ alloy respectively.

The formation of FCC hydrides in similar BCC HEA systems has been reported in the literature [24,8,9]. Silva *et al.* [24] studied three different compositions of the TiVNbM (M = Cr, Co, Ni) system that presented hydrogen storage capacities of the same order as those observed here (*i.e.* around 3.11-3.18 wt.%). However, they apply a heat treatment at 390°C under dynamic vacuum for 12h to facilitate hydrogen absorption.

Table 4 - Lattices parameters, cell volume and H/M calculated for the hydrides formed.

Composition (Hydride)	Structure	Lattices parameters Å	cell volume Å^3	cell volume/Z	H/M
$Ti_{35}V_{35}Nb_{20}Cr_5Mn_5$	FCC	4.414	86.00	21.50	1.5
$Ti_{32}V_{32}Nb_{18}Cr_9Mn_9$	FCC	4.394	84.82	21.20	1.2
$Ti_{27.5}V_{27.5}Nb_{20}Cr_{12.5}Mn_{12.7}$	FCC	4.385	84.30	21.07	2.1

The hydrogen absorption capacity of the BCC HEA alloys has been discussed based on some HEA parameters, such as the valence electron concentration (VEC) [29] and on the δ parameter [6,30], related to the atomic size mismatch, and whose association with the level of local distortion has been demonstrated [32].

Concerning the VEC effect, it has been demonstrated that increasing VEC, the volumetric cell expansion per atom of hydrogen is increased while the thermal stability of the formed hydride is decreased [33]. Nygard *et al.* [33] had proposed that a larger fraction of the interstitial sites is occupied by hydrogen atoms when the VEC of the nearest neighbors is lower (at the local level). This could indicate that a lower VEC would promote an increase in storage capacity, but, in this case, the stability of hydrides would be higher, limiting the reversible storage capacity. So, a balance between maximum storage capacity and reversible capacity could be tuned by VEC. Nygard *et al*. [29] proposed that alloys with VEC < 4.75 reached maximum capacity of 2 H/M, whereas alloys with VEC > 5 presented reduced maximum capacity (H/M < 2.0), indicating the formation of non-stoichiometric hydride for these larger VEC. For the alloys studied in this work, the VEC values increased from 4.8 to 5.1 with increasing levels of Cr and Mn. These results, therefore,

are not in agreement with those proposed by Nygard *et al*. [29], since the alloy with the highest VEC (5.1) was the one with the highest absorption capacity despite the longer incubation time.

Sahlberg *et al*. [15] argued that the strain in the HEA could be a driving force to open new interstitial sites for hydrogen and that higher hydrogen storage capacities should be an effect of the distorted HEA lattice. However, later works [34,35] did not find a clear mechanism to link δ with both the lattice distortion and hydrogen storage capacity. In this work, δ values range from 5.13 to 5.47, increasing with the Cr and Mn contents, and in agreement with values discussed by Sahlberg *et al*. [15], being the higher δ associated to higher hydrogen capacity.

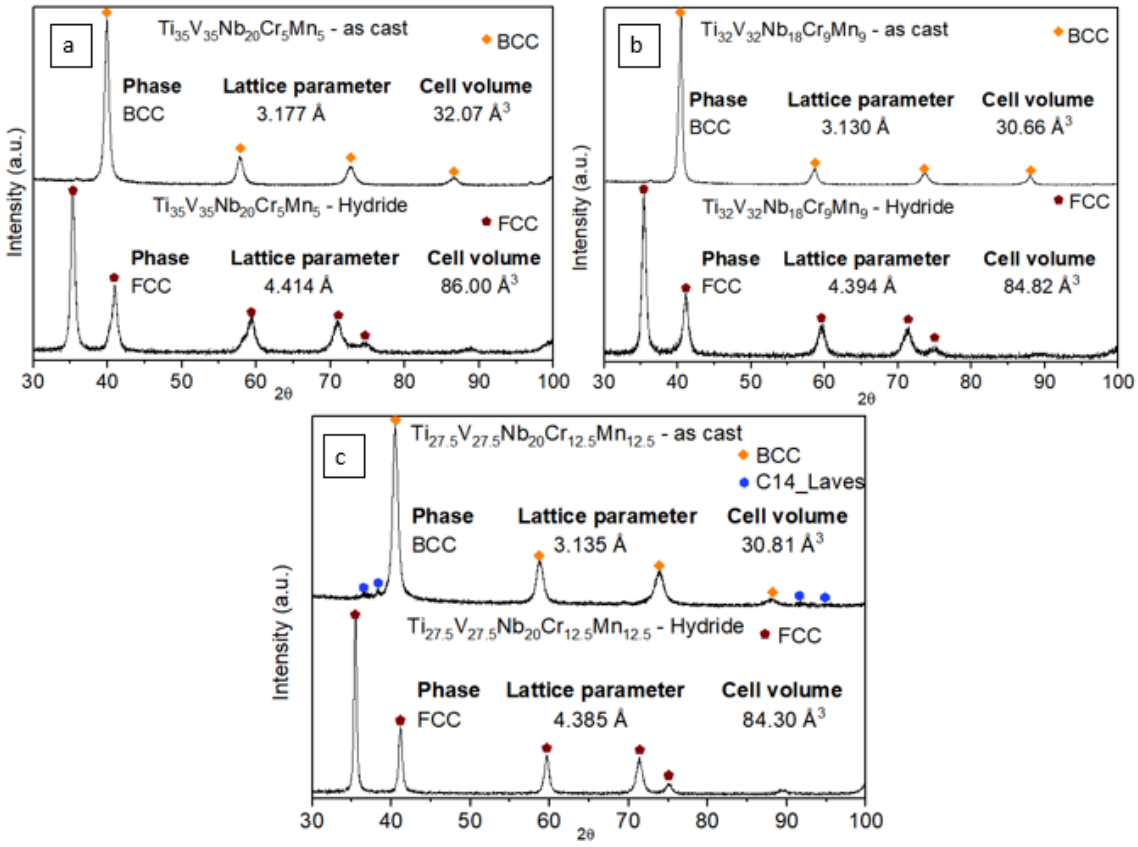

Figure 5. Comparison XRD patterns of the $Ti_{35}V_{35}Nb_{20}Cr_5Mn_5$ (a), $Ti_{32}V_{32}Nb_{18}Cr_9Mn_9$ (b) and $Ti_{27.5}V_{27.5}Nb_{20}Cr_{12.5}Mn_{12.5}$ (c) alloys in as-cast condition with the BCC phase and after the activation with the hydride FCC phase.

After the activation, the $Ti_{32}V_{32}Nb_{18}Cr_9Mn_9$ and the $Ti_{27.5}V_{27.5}Nb_{20}Cr_{12.5}Mn_{12.5}$ alloys were subjected to three more hydrogenation/dehydrogenation cycles. Cycling was performed with fresh samples, and the results are shown in Figure 6.

The $Ti_{32}V_{32}Nb_{18}Cr_9Mn_9$ alloy showed a different behavior in the cycles subsequent to activation, the 2nd hydrogen absorption, reaching a relatively higher amount of hydrogen, about 2.72wt.% and increased in the 3rd absorption to 2.99wt.% (Figure 6a). However, it was reduced in the 4th absorption cycle reaching 2.66 wt.% due a possible incomplete desorption between the 3rd and the 4th cycle, but it is difficult to explain why just for the for the 4th absorption, it is still unclear.

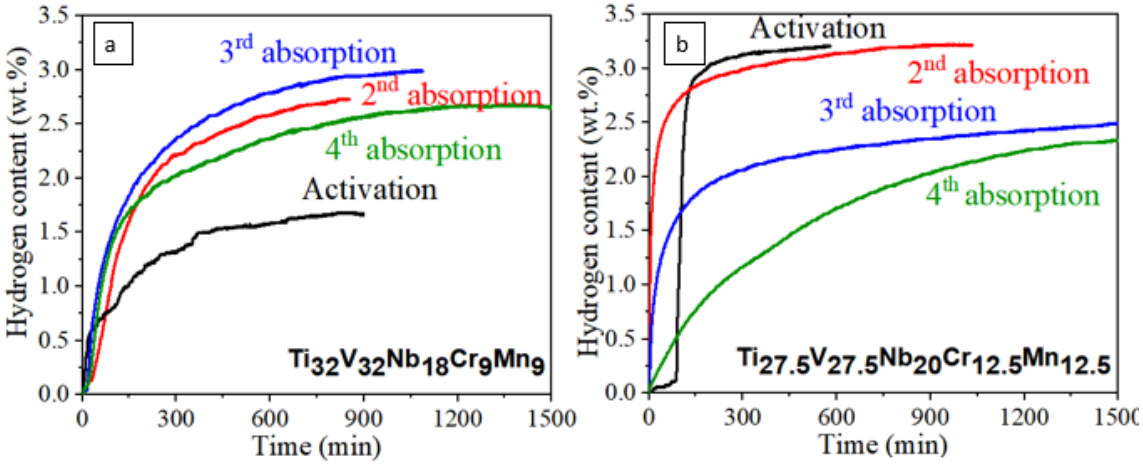

Figure 6. Four cycles of absorption (room temperature 2MPa)/desorption (300°C under dynamic vacuum) (a) $Ti_{32}V_{32}Nb_{18}Cr_9Mn_9$ and (b) $Ti_{27.5}V_{27.5}Nb_{20}Cr_{12.5}Mn_{12.5}$.

The $Ti_{27.5}V_{27.5}Nb_{20}Cr_{12.5}Mn_{12.5}$ alloy behaves differently from the $Ti_{32}V_{32}Nb_{18}Cr_9Mn_9$ alloy. The highest hydrogen capacity was obtained during the activation, 3.20 wt.%, with an incubation time of around 100 minutes (Figure 6-b). The 2nd absorption had faster kinetics and the capacity was almost the same as that obtained during activation. On the other hand, it is observed that the curves of the 3rd and 4th absorptions present quite different results, with low capacities and kinetics.

The Figure 7 presents the XRD patterns of $Ti_{27.5}V_{27.5}Nb_{20}Cr_{12.5}Mn_{12.5}$ alloy samples after the activation, after the 4th absorption and in the desorbed condition after the 4th desorption. The lattice parameters and cell volumes calculated from these XRD patterns are shown in Table 5. It is clear from these results that the same FCC hydride phase is present after the activation (1st hydrogenation) and after the 4th absorption, with almost the same lattice parameter (4.385 to 4.391). However, a very low intensity peak is observed in the diffractogram obtained from the sample after the 4th absorption, indicating a possible formation of another phase, a hydride with BCT structure. This hydride can be formed during the first hydrogenation step. The lattice parameters and unit cell volume obtained by Rietveld refinement for this BCT phase are also shown in Table 5.

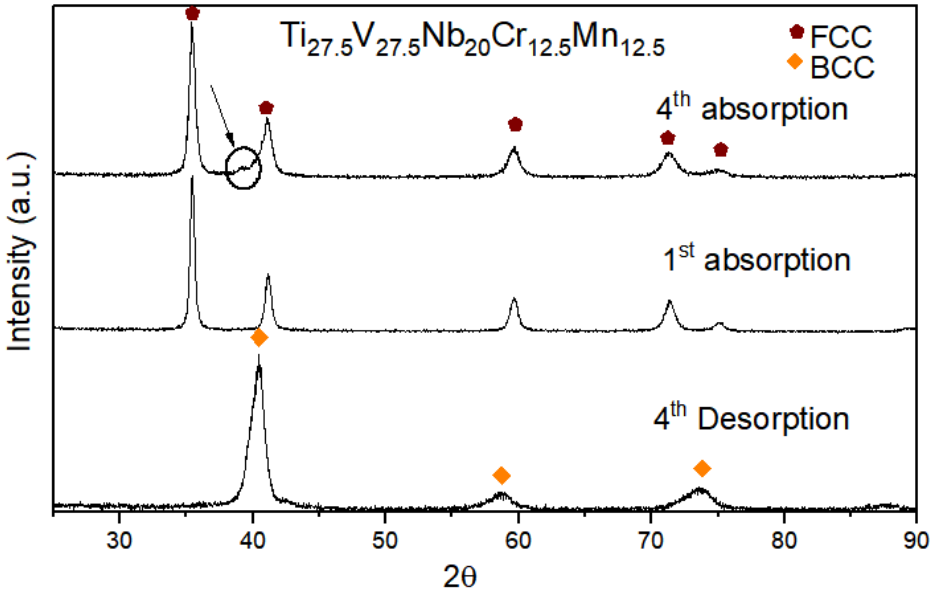

Figure 7. Comparison XRD patterns of the $Ti_{27.5}V_{27.5}Nb_{20}Cr_{12.5}Mn_{12.5}$ alloy after 1st absorption, 4th absorption and 4th desorption.

The results suggest that the absorption capacity of the alloy after the 4th cycle remains similar to the initial one. In this case, the curves of the 3rd and 4th absorptions show only an apparent lower hydrogen capacity (Figure 6-b) due to the incomplete previous hydrogen desorption, i.e. the absorption in the 3rd and 4th cycles would start with some retained hydrogen content (wt.%) in the sample. The broadened peaks of the BCC phase in the diffractograms of sample after desorption support this hypothesis (Figure 7).

Table 5 - Comparison of the hydride formation parameters after the 1st absorption, 4th absorption and 4th desorption.

$Ti_{27.5}V_{27.5}Nb_{20}Cr_{12.5}Mn_{12.5}$ samples	**Phase**	**Lattice parameter (Å)**	**Cell volume (Å³)**
1st absorption	FCC	4.385	84.30
After 4th absorption	FCC (89%)	4.391	84.66
	BCT (11%)	a = 3.240 c = 3.061	32.13
4th desorption	BCC	3.150	31.21

Recently, Liu *et al*. [8] studied the hydrogen properties in alloys with similar composition to those studied in this work, containing BCC phase as the main phase, and some amount of intermetallic AB_2 and Ti phases due to the great difference in atomic radius of the elements. It has been shown that the presence of these secondary phases can reduce the hydrogen storage capacity. However, in the present work, the $Ti_{27.5}V_{27.5}Nb_{20}Cr_{12.5}Mn_{12.5}$ alloy, which contains about 6% of the Laves phase, achieved the highest hydrogen storage capacity. In another work, Liu *et al*. [9] also compared the kinetics of absorption in Ti-V-Cr alloys, showing that the kinetics increases with increasing cell volume for the BCC alloys. However, these authors reported that some alloys with smaller cell volume showed faster hydrogen absorption than some others due to the presence of a secondary phase that provides tunnels for hydrogen diffusion. Among the three alloys studied in this work, the $Ti_{27.5}V_{27.5}Nb_{20}Cr_{12.5}Mn_{12.5}$, with some amount of Laves phase, presented the highest hydrogen capacity and the fastest kinetics, indicating that the presence of this phase in low quantities can improve the kinetics helping in reaching maximum hydrogen capacities for this alloy.

4. **Conclusions**

The $Ti_{35}V_{35}Nb_{20}Cr_5Mn_5$, $Ti_{32}V_{32}Nb_{18}Cr_9Mn_9$ and $Ti_{27.5}V_{27.5}Nb_{20}Cr_{12.5}Mn_{12.5}$ alloys were designed by thermodynamical calculations to be formed by BCC solid solutions with a small amount of the Laves phase, and produced by arc melting.

The alloys in as-cast condition present the phases according to the predictions of the Thermo-Calc calculations. The three alloys compositions presented a dendritic microstructure formed by solid solutions with BCC crystalline structure. Small precipitates, mainly in the interdendritic regions, identified by XRD as the C14 Laves phase, were observed in the $Ti_{27.5}V_{27.5}Nb_{20}Cr_{12.5}Mn_{12.5}$ alloy.

The alloys have a high capacity for hydrogen absorption, the highest being obtained for the $Ti_{27.5}V_{27.5}Nb_{20}Cr_{12.5}Mn_{12.5}$ alloy, 3.45 wt.% corresponding to H/M = 2.1. The absorption takes place at room temperature, which is interesting from a technological point of view, without the need for previous high temperature heat treatments. The cycling of the $Ti_{32}V_{32}Nb_{18}Cr_9Mn_9$ alloy shows the best kinetics after the activation and also the highest values of the maximum capacity.

The apparent decrease in kinetics and maximum hydrogen storage capacity of the $Ti_{27.5}V_{27.5}Nb_{20}Cr_{12.5}Mn_{12.5}$ alloy after cycling can be explained by the incomplete desorption of the alloy after the 2nd cycle.

5. References

[1] A . Zuttel , A . Borgschulte , L. Schlapbach , Hydrogen as a Future Energy Carrier, Wiley VCH Press, Germany, 2008 .

[2] N. Rusman , M. Dahari , Int. J. Hydrogen Energy 41 (2016) 12108–12126 .

[3] Yeh JW, Chen SK, Lin SJ, Gan JY, Chin TS, Shun TT, Tsau CH, Chang SY. Nanostructured high-entropy alloys with multiple principal elements: Novel alloy design concepts and outcomes. Advanced Engineering Materials. 6 (2004) 299-303.

[4] Zhang Y, Zhou YJ, Lin JP, Chen GL, Liaw PK. Solid-Solution Phase Formation Rules for Multi-component Alloys. Advanced Engineering Materials. 10 (2008) 534–538.

[5] Senkov ON, Senkova SV, Miracle B, Woodward C. Mechanical properties of low-density, refractory multi-principal element alloys of the Cr–Nb–Ti–V–Zr system. Materials Science and Engineering: A. 565 (2013) 51–61.

[6] Guo S, Ng C, Lu J, Liu CT. Effect of valence electron concentration on stability of fcc or bcc phase in high entropy alloys. Journal of Applied Physics. 109 (2011) 103505.

[7] Yeh JW, Lin SJ, Chin TS, Gan JY, Chen SK, Shun TT, et al. Formation of simple crystal structures in Cu–Co–Ni–Cr–Al–Fe–Ti–V alloys with multiprincipal metallic elements. *Metallurgical* and *Materials Transactions A*. 35(8) (2004) 2533–2536.

[8] Jingjing Liu, Jie Xu, Salma Sleiman, Francia Ravalison, Wei Zhu, Hongfei Liu, Honghui Cheng, Jacques Huot, Hydrogen storage properties of V0.3Ti0.3Cr0.25Mn0.1Nb0.05 high entropy alloy, International Journal of Hydrogen Energy,Volume 47, Issue 61 (2022) 25724-25732.

[9] Jingjing Liu, Jie Xu, Salma Sleiman, Xiangyu Chen, Shuai Zhu, Honghui Cheng, Jacques Huot, Microstructure and hydrogen storage properties of Ti–V–Cr based BCC-type high entropy alloys, International Journal of Hydrogen Energy, Volume 46, Issue 56 (2021) 28709-28718.

[10] Wu JM, Lin SJ, Yeh JW, Chen SK, Huang YS, Chen HC. Adhesive wear behavior of AlxCoCrCuFeNi high-entropy alloys as a function of aluminum content. Wear. 261 (5-6) (2006) 513–519.

[11] Varalakshmi S, Kamaraj M, Murty BS. Synthesis and characterization of nanocrystalline AlFeTiCrZnCu high entropy solid solution by mechanical alloying. Journal of Alloys and Compounds. 460 (2008) 253-257.

[12] Wang XF, Zhang Y, Qiao Y, Chen GL. Novel microstructure and properties of multicomponent CoCrCuFeNiTix alloys. Intermetallics 15 (2007) 357-362.

[13] He JY, Liu WH, Wang H, Wu Y, Liu XJ, Nieh TG, et al. Effects of Al addition on structural evolution and tensile properties of the FeCoNiCrMn high-entropy alloy system Acta Materialia. 62 (2014) 105-113.

[14] Ma SG, Zhang Y. Effect of Nb addition on the microstructure and properties of AlCoCrFeNi high-entropy alloy Materials Science and Engineering: A. 532 (2012) 480-486.

[15] Sahlberg M, Karlsson D, Zlotea C, Jansson U. Superior hydrogen storage in high entropy alloys. Sci Rep 6 (2016) 1-6.

[16] Kunce I, Polanski M, Bystrzycki J. Microstructure and hydrogen storage properties of a TiZrNbMoV high entropy alloy synthesized using Laser Engineered Net Shaping (LENS). International Journal of Hydrogen Energy, 39 (2014) 9904-9910.

[17] Gao MC Miracle DB, Maurice D, Yan X, Zhang Y, Hawk JA. High-entropy functional materials. J. Mater. Res. 2018, 1–18.

[18] Kunce I, Polanski M, Bystrzycki J. Structure and hydrogen storage properties of a high entropy ZrTiVCrFeNi alloy synthesized using Laser Engineered Net Shaping (LENS). Int J Hydrogen Energy, v. 38 (2013) 12180-12188.

[19] Karlsson D, Ek G, Cedervall J, Zlotea C, Moller KT, Hansen TC, Bednarcik J, Paskevicius M, Sorby MH, Jensen TR, Jansson U, Sahlberg M. Structure and Hidrogenation Properties of a HfNbTiVZr Entropy Alloy. Inorganic Chemistry 57 (2018) 2103-2110.

[20] Chen SK, Lee PH, Lee H, Su HT. Hydrogen storage of C14-CruFevMnwTixVyZrz alloys. Mat. Chemistry and Physics 210 (2018) 336-347.

[21] Shen H, Zhang J, Hu J, Zhang J, Mao Y, Xiao H, Zhou X, Zu X. A novel TiZrHfMoNb high entropy alloy for solar thermal energy storage. Nanomaterials 9 (2019).

[22] Miraglia S, Fruchart D, Skryabina N, Shelyapina M, Ouladiaf B, Hlil EK, Rango P, Charbonnier J. Hydrogen-induced structural transformation in TiV0.8Cr1.2 studied by in situ neutron diffraction, J. Alloys Compd. 442 (2007) 49–54.

[23] Kao YF, Chen SK, Sheu JH, Lin JT, Lin WE, Yeh JW, et al. Hydrogen storage properties of multi-principal-component CoFeMnTixVyZrz alloys. Int J Hydrogen Energy, v.35 (2010) 9046-9059.

[24] B. Silva, C. Zlotea, Y.Champion, W. Botta, G. Zepon, Design of TiVNb-(Cr, Ni or Co) multicomponent alloys with the same valence electron concentration for hydrogen storage, Journal of Alloys and Compounds,Volume 865, (2021).

[25] Edalati P, Floriano R, Mohammadi A, Li Y, Zepon G, Li H-W, Edalati K. Reversible room temperature hydrogen storage in high-entropy alloy TiZrCrMnFeNi. Scripta Materialia 178 (2020) 387–390

[26] Toby, B. H., & Von Dreele, R. B. (2013). "GSAS-II: the genesis of a modern open-source all purpose crystallography software package". *Journal of Applied Crystallography*, **46**(2), 544-549. doi:10.1107/S0021889813003531

[27] I. Kunce, M. Polanski, J. Bystrzycki, Structure and hydrogen storage properties of a high entropy ZrTiVCrFeNi alloy synthesized using Laser Engineered Net Shaping (LENS), International Journal of Hydrogen Energy, Volume 38, Issue 27, 2013, Pages 12180-12189,

[28] S. Yang, F. Yang, C. Wu, Y. Chen, Y. Mao and L. Luo, J. Alloys Compd., 2016, 663, 460–465.

[29] Nygård MM, Ek G, Karlsson D, Sørby MH, Sahlberg M, Hauback BC. Counting electrons - A new approach to tailor the hydrogen sorption properties of high-entropy alloys. Acta Materialia 175 (2019) 121-129.

[30] Y.F. Ye, Q. Wang, J. Lu, C.T. Liu, Y. Yang, High-entropy alloy: challenges and prospects, Mater. Today 19 (2016) 349e362.

[31] S. Guo, C.T. Liu, Phase stability in high entropy alloys: formation of solid-solution phase or amorphous phase, Progr. Nat. Sci.: Mater. Int. 21 (2011) 433–446.

[32] M. M. Nygard, W. A. Sławin´ski, G. Ek, M. H. Sorby, M. Sahlberg, D. A. Keen and B. C. Hauback, Acta Mater., 2020, 199, 504–513.

[33] G. Ek, M. M. Nygard, A. F. Pavan, J. Montero, P. F. Henry, M. H. Sorby, M. Witman, V. Stavila, C. Zlotea, B. C. Hauback and M. Sahlberg, Inorg. Chem., 2020,60(2), 1124–1132.

[34] M. M. Nygard, G. Ek, D. Karlsson, M. Sahlberg, M. H. Sorby and B. C. Hauback, Int. J. Hydrogen Energy, 2019, 44, 29140–29149.

[35] M. M. Nygard, O. S. Fjellvag, M. H. Sorby, K. Sakaki, K. Ikeda, J. Armstrong, P. Vajeeston, W. A. Sławin´ski, H. Kim, A. Machida, Y. Nakamura and B. C. Hauback, Acta Mater., 2020, 116496.

[36] Kao, Y.F., Chen, S.K., Sheu, J.H., Lin, J.T., Lin, W.E., Yeh, J.W., Lin, S.J., Liou, T.H. and Wang, C.W. (2010) Hydrogen Storage Properties of Multi-Principal-Component CoFeMnTixVyZrz Alloys. International Journal of Hydrogen Energy, 35, 9046-9059.

[37] C. Ng, S. Guo, J. Luan, S.Shi, C.T. Liu. Entropy-driven phase stability and slow diffusion kinetics in an Al0.5CoCrCuFeNi high entropy alloy, Intermetallics 31 (2012) 165-172.

[38] S.Sleiman and J. Huot, J. Microstructure and First Hydrogenation Properties of TiHfZrNb1-xV1+x Alloy for x = 0, 0.1, 0.2, 0.4, 0.6 and 1. Alloys Compd., 2021, 861, 158615

[39] Zhang, B.; Tang, Y.; Li, S.; Ye, Y.; Zhu, L.; Zhang, Z.; Liu, X.; Wang, Z.; Bai, S. Effect of Ti on the Structure and Mechanical Properties of TixZr2.5-xTa Alloys. *Entropy* 2021, *23*, 1632.